# Geostrophic Scatter Diagrams and the Application of Quasigeostrophic Free-Mode Theory to a Northeast Pacific Blocking Episode

NILS R. EK

*Division of Meteorology, Department of Geography, University of Alberta, Edmonton, Alberta, Canada*

GORDON E. SWATERS

*Applied Mathematics Institute, Department of Mathematics, and Institute of Geophysics, Meteorology and Space Physics, University of Alberta, Edmonton, Alberta, Canada*

(Manuscript received 2 April 1992, in final form 25 June 1993)

ABSTRACT

Throughout the latter part of January and most of February 1989 a large-scale intense blocking event occurred over the northeast Pacific Ocean. During its lifetime the block exhibited two distinct spatial configurations corresponding to Omega and dipole shapes, respectively. A time series of scatter diagrams of 5-day-averaged 500-mb geostrophic streamfunction versus potential vorticity ($\psi$ vs $q$) is computed. It is suggested that both the Omega and dipole forms may correspond to free modes. It is shown that immediately *prior* to the block formation there is a rapid steepening of the $q(\psi)$ scatter diagrams associated with a strong increase in net vorticity being advected out of the block region. A suggestion is made that this analysis may be useful in identifying flow configurations that are capable of initiating blocks. It is possible to separate the geostrophic streamfunction into a product of horizontal and vertical components. The vertical structure problem is solved analytically using a constant lapse rate approximation for the background atmosphere, and a constant value for the gradient of the mean flow potential vorticity with respect to the geostrophic streamfunction. It is shown that as the block develops, the contribution of the gravest, quasi-barotropic mode dramatically increases and forms the dominant mode. Immediately prior to the formation of the dipole configuration, a small increase in baroclinicity was observed near the block interior. It is suggested that this event could be evidence of eddy forcing similar to that proposed for the maintenance of North Atlantic dipole blocks.

## 1. Introduction

Over the past decade, attempts have been made to model atmospheric blocking using idealized solutions of the quasigeostrophic equations that can persist for times comparable to blocking durations. Because the time scale associated with a block [on the order of about 10 days; see Rex (1950)] and the horizontal amplitudes are larger than that typically associated with transient baroclinic disturbances, a reasonable conjecture is that blocking may correspond to the atmosphere, attempting to configure itself into a localized, finite-amplitude free mode (i.e., a steady, nonlinear exact solution) that is rather stable to smaller eddy disturbances. The soliton (Malguzzi and Malanotte-Rizzoli 1984; Warn and Brasnett 1983) and the modon (McWilliams 1980; Butchart et al. 1989; Haines and Marshall 1987; Haines 1989) are two models that have received considerable attention. In quasigeostrophic dynamics, a free mode is characterized formally by a functional relation $q = q(\psi)$, where $q$ is the potential vorticity and $\psi$ the streamfunction.

One way of testing whether or not a particular observed flow pattern is developing into a free mode is to examine the *geostrophic scatter diagrams* for the flow (see Read et al. 1986). Scatter diagrams are simply two-dimensional scatterplots of the observed streamfunction versus the observed potential vorticity from many points within a given geographical region at a given height. For example, the scatter diagram associated with the modon is a simple multivalued pattern comprising two distinct lines corresponding to the interior and exterior regions, respectively (Stern 1975; Flierl et al. 1980). Read et al. (1986) presented a technique for computing the area associated with a given scatter diagram. For a free mode, the scatterplot collapses onto a curve, and the area *must* be identically zero because the integrated or net flux of vorticity is zero; see section 3d. The *observed* scatter diagram area can therefore be viewed as a measure of the degree of departure of the observed flow from a quasigeostrophic free-mode state.

*Corresponding author address:* Dr. Gordon E. Swaters, Department of Mathematics, Applied Mathematics Institute, University of Alberta, 632 Central Academic Building, Edmonton, Alberta, Canada, T6G 2G1.
E-mail: gordan@hamal.math.ualberta.ca.

Butchart et al. (1989) presented a theoretical and diagnostic study of an atmospheric block over central Europe. One of the most important conclusions of their study was the clear indication of the development of a simple nonanalytic pattern in the scatter diagrams that had a striking resemblance to the scatter diagram for a geostationary modon solution. One of the principal purposes of this paper is to present the results of a similar study for a blocking episode that occurred throughout the latter part of January and most of February 1989 over the northeast Pacific Ocean.

This blocking episode is notable not only for its duration and its large horizontal amplitude (see Fig. 1) but also for the configurations it assumed. Typically, blocks over the northeast Pacific differ from European (or Atlantic) blocks in that they tend to form an Omega configuration (see, e.g., Mullen 1986, 1987). Atlantic blocks can often take the form of a meridionally aligned dipole configuration. The Pacific block that is studied here initially developed into the more familiar Omega configuration that persisted from about 1 to 14 February. However, from the 14th to about the 18th the block appeared to evolve into a dipole configuration, which lasted until about 21 February when the block episode completely subsided.

The time series of 5-day-averaged scatter diagrams that we present shows a qualitative trend toward a multivalued configuration in which the plots of $q$ versus $\psi$ appear to steepen. Our results show a very distinct tendency for the magnitude of the net vorticity flux to decrease as the block develops, strongly suggesting that the blocking configuration observed is more free mode–like than either the pre- or postblock configurations.

We also attempt to make a highly qualitative assessment of the stability tendencies of the Omega and dipole configurations by comparing least-square estimates of the slopes of the scatter diagrams against a proxy Arnol'd's stability criterion (Arnol'd 1966; McIntyre and Shepherd 1987). During the onset of the Omega configuration there appears to be a tendency toward stability. However, during the onset of the dipole configuration this tendency is reversed. This may help to explain why the length of time the dipole configuration is observed is much shorter than the length of time the Omega configuration is observed.

The baroclinic evolution of the block is also examined. Our results show a distinct tendency toward a quasi-barotropic configuration as the block develops. This barotropic configuration is maintained throughout the life of the block. However, immediately prior to the formation of the dipole block we can identify a brief period with a slight increase in baroclinic activity associated with a transient cyclone. It is interesting to speculate that this baroclinic activity is associated with the eddy-straining process proposed by Shutts (1983, 1986) as a mechanism for driving atmospheric blocks into a dipole configuration.

The plan of this paper is as follows. In section 2, the dataset we used is briefly described and the method of computing the various dynamical quantities of interest is outlined. In addition, we give a brief synopsis of the events that lead to the formation of this particular northeast Pacific block episode.

In section 3 the main theoretical aspects of the paper are presented. We present an isolated geostationary blocking eddy solution that is embedded in vertically stratified westerly flow having no meridional shear, as-

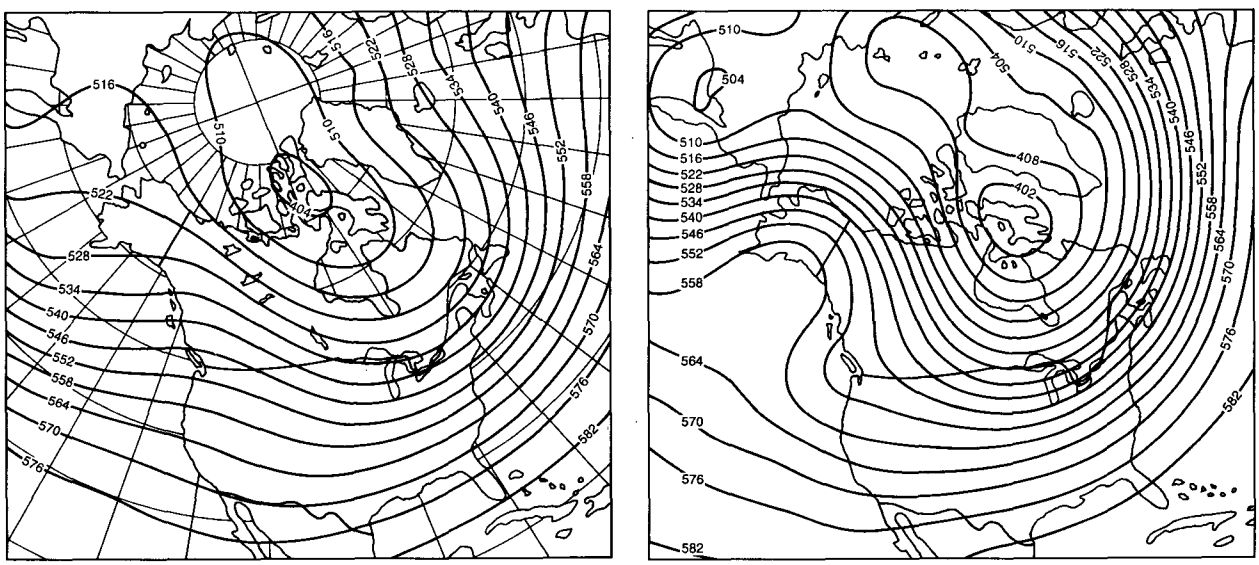


FIG. 1. Mean 500-mb geopotential height (dam) for February: (a) climatological average; (b) February 1989. Adapted from Canadian Meteorological Centre (1989).

suming a power law form for the static stability. As well, we describe some of the theoretical aspects of geostrophic scatter diagrams that are required in the subsequent analysis.

In section 4, we apply the theoretical modeling to the observed block. Several calculations are presented, beginning with the estimates required of the parameters that are needed in the modeling work. The solution to the vertical mode problem is discussed. The time series of the geostrophic scatter diagrams is presented and discussed, as is the computed time series of vorticity flux. A time series of least-square estimates for the slopes of the $q(\psi)$ scatter diagrams is given. Based on this calculation, inferences are made with respect to the stability characteristics of the observed block. The paper is summarized in section 5.

## 2. The Pacific block of February 1989

### a. The dataset

The data (supplied by the Canadian Meteorological Centre) consist of objectively analyzed archived data on a latitude–longitude grid, at a two-degree spacing. The full grid extends from 30° to 80°N and westward from 20°W to 120°E (see Fig. 2). Five levels were used: 850, 700, 500, 400, and 250 mb. At each level, three data fields were used: the geopotential height of the pressure surface denoted as $Z$; the temperature denoted as $T$; and the dewpoint depression given by $T - T_d$. There are normally four datasets for each day (one for every 6 hours), running for 39 days from 21 January through 28 February 1989. The initial preparation consisted of time averaging (at each grid point) each data field, over the four synoptic periods per day. This smoothed out the smallest-scale disturbances.

The geostrophic streamfunction was calculated at each grid point $(i, j)$ as $\psi_{i,j} \equiv f_0^{-1} g Z_{i,j}$, where $f_0$ is the Coriolis parameter at 60°N, $g$ is the gravitational acceleration, and $Z_{i,j}$ is the geopotential height of the isobaric surface. The vertical component of absolute vorticity was calculated as $\nabla^2\psi_{i,j} + f$, using the following centered finite-difference scheme for the Laplacian term:

$$\nabla^2\psi_{i,j} \approx \frac{\psi_{i,j+1} + \psi_{i,j-1} - 2\psi_{i,j}}{\delta x_i^2} + \frac{\psi_{i+1,j} + \psi_{i-1,j} - 2\psi_{i,j}}{\delta y^2}.$$

In this expression $\delta y$ is the (constant) north–south grid spacing. The zonal grid spacing $\delta x_i$ is not constant on our lat–long projection. We employ throughout our work the beta-plane approximation

$$f = f_0 + \beta y.$$

The baroclinic stretching term in the potential vorticity [see (3.2)] was computed using a finite-difference approximation of the term (as in Hoskins et al. 1985)

$$f_0 \frac{\partial}{\partial p}\left(\frac{\theta^*}{d\theta_r/dp}\right),$$

where $\theta^* = \theta^*(x, y, p)$ is the deviation from the area-averaged virtual potential temperature $\theta_r$.

We applied first a spatial and then a temporal smoother to the vorticity and streamfunction fields. The spatial smoother is a simple 5-point smoother, weighted to take into account the variable zonal grid spacing. The fields were then time averaged over 5 days, with equal weights. All calculations in this paper begin with the 5-day mean fields, each centered on the date listed.

Throughout this study, the region occupied by the block was approximated by a horizontal box-shaped area, bounded by the latitudes 46° and 70°N and longitudes 114° and 166°W. This box shape was subjectively chosen to surround, as closely as possible, the portion of the block having closed streamfunction and vorticity contours, on as many days as possible.

### b. Synopsis

Prior to the block's formation, a strongly baroclinic situation was in place over North America. A zonal flow of quite mild Pacific air persisted over western and central Canada, while a very cold air mass lay over the Arctic, where record-setting minimum temperatures and maximum barometric pressures were recorded, no-

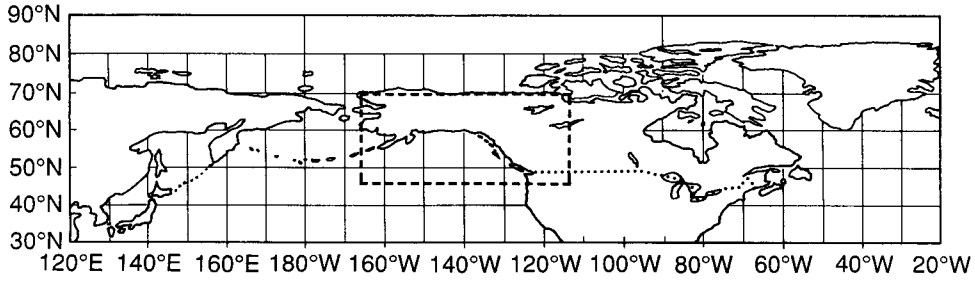


FIG. 2. The region covered by the data. The box over the Gulf of Alaska approximates the block's interior.

tably the highest surface pressure reading in North America—1074.8 mb—at Northway, Alaska, on 31 January 1989. Refer to Fig. 3a for the departure from normal of surface temperature.

In the first few days of February, a blocking ridge formed quickly over the northeast Pacific after a large, intense cyclonic system left the Gulf of Alaska and tracked across western Canada and the United States (see Fig. 4a). This resulted in a surge of arctic air that reached the West Coast and covered all but the southernmost U.S. states. The block was characterized, in the lower troposphere, by a very strong horizontal thermal contrast between its mild Pacific flank and the cold northwesterly stream farther east over central North America. Referring to Fig. 3b, we can see that during the second week in February, record mild temperatures were observed over Yukon, while near-record low temperatures were experienced over southwestern Canada and the United States (Canadian Climate Centre 1989).

Based on the series of 5-day mean 500-mb charts, we may subjectively consider the block to have evolved between two states. From about 1 to 14 February, the flow pattern had the familiar Omega ($\Omega$) shape (see Figs. 4a–c). During the second, shorter period, 18 to 21 February, shortly before it broke down, the block developed a discernible dipolelike form (see Figs. 4f–i). Selected charts are given in Fig. 4. The full series of 500-mb charts is given in Ek (1992).

## 3. Theoretical considerations

### a. *Problem formulation*

We use dimensional variables throughout our analysis. We begin with the equation for the steady, source-free, quasigeostrophic potential vorticity on a beta plane (Pedlosky 1987) written with respect to pressure coordinates in the form

$$J(\psi, q) \equiv \frac{\partial \psi}{\partial x}\frac{\partial q}{\partial y} - \frac{\partial \psi}{\partial y}\frac{\partial q}{\partial x} = 0, \qquad (3.1)$$

in which $\psi$ is the geostrophic streamfunction, given by

$$\psi \equiv \phi / f_0,$$

where $\phi$ is the geopotential. The directions of the Cartesian coordinates $x$ and $y$ are east and north, respectively. The quasigeostrophic potential vorticity, $q$, is given by

$$q = \nabla^2 \psi + \beta y + f_0^2 \frac{\partial}{\partial p}\left(\frac{1}{\sigma_r}\frac{\partial \psi}{\partial p}\right), \qquad (3.2)$$

and the static stability parameter, $\sigma_r$, is defined to be

$$\sigma_r = -\frac{1}{\rho_r \theta_r}\frac{d\theta_r}{dp},$$

in which $\theta_r(p)$ is a reference potential temperature distribution, and $\rho_r$ is a reference density. The appropriate vertical boundary conditions are discussed in section 3c. Appropriate horizontal boundary conditions on the solution to (3.1) will be described in the next section. It follows immediately from (3.1) that

$$q = \mathcal{F}(\psi), \qquad (3.3)$$

in which the function $\mathcal{F}$ is for now left unspecified.

### b. *Mean flow and block decomposition*

The solution described here corresponds to a stationary isolated anomaly embedded in a stratified zonal flow having no meridional shear. The solution procedure follows that of Haines and Marshall (1987), and

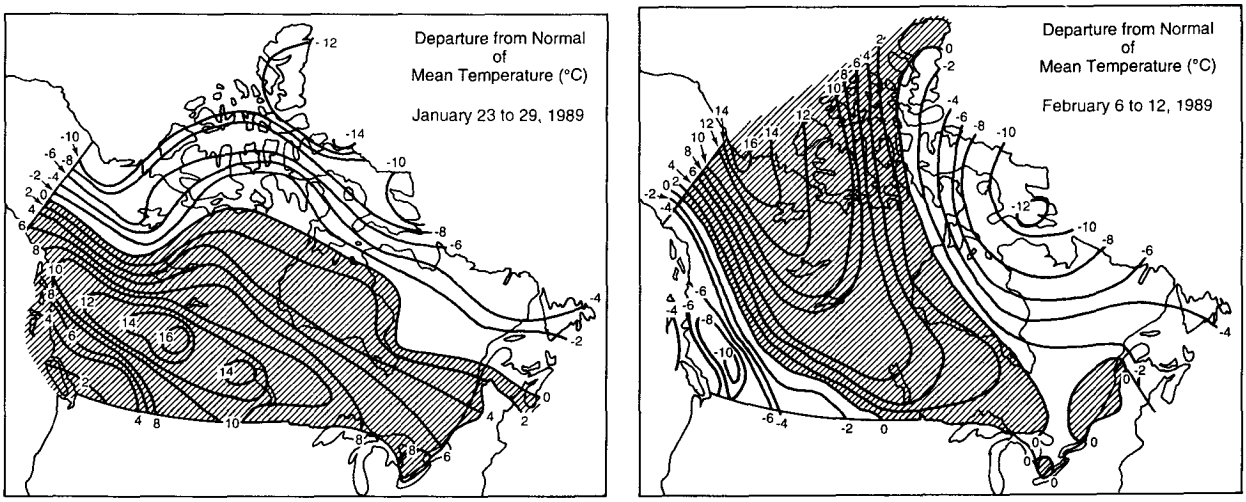


FIG. 3. Average departure (°C) from normal temperature (a) 23–29 January 1989; (b) 6–12 February 1989. Adapted from Canadian Climate Centre (1989).

full details are presented by Ek (1992). We assume that both the streamfunction and vorticity can be expressed as linear combinations of a zonal background plus eddy field, in the form

$$\psi = \psi_0(y, p) + \psi_1(x, y, p), \quad (3.4a)$$

$$q = q_0(y, p) + q_1(x, y, p), \quad (3.4b)$$

so that we may rewrite (3.3) as

$$q_0 + q_1 = \mathcal{F}(\psi_0 + \psi_1). \quad (3.5)$$

We note that $\psi$ in (3.4a) is the total dynamic anomaly, that is, the departure from a hydrostatic reference state (Pedlosky 1987). The background zonal flow streamfunction is assumed to be of the form

$$\psi_0 = -U(p)y, \quad U(p) > 0, \quad (3.6)$$

which corresponds to a vertically sheared westerly flow with no horizontal shear. The background and eddy components of potential vorticity, as defined by (3.2), are given by

$$q_0 = \beta y - f_0^2 \frac{\partial}{\partial p}\left(\frac{1}{\sigma_r}\frac{dU(p)}{dp}y\right), \quad (3.7)$$

$$q_1 = \nabla^2\psi_1 + f_0^2 \frac{\partial}{\partial p}\left(\frac{1}{\sigma_r}\frac{\partial \psi_1}{\partial p}\right), \quad (3.8)$$

respectively.

A solution for the eddy field can be obtained in the separable form

$$\psi_1 = \Psi(p)\tilde{\psi}(x, y), \quad (3.9)$$

where $\Psi(p)$ is the vertical structure function. Substitution of (3.9) into (3.8) leads to

$$q_1 = \Psi\nabla^2\tilde{\psi} + f_0^2\tilde{\psi}\frac{\partial}{\partial p}\left(\frac{1}{\sigma_r}\frac{\partial \Psi}{\partial p}\right). \quad (3.10)$$

Substituting into (3.5) for $\psi_0$, $q_0$, $\psi_1$, and $q_1$ from (3.6) through (3.10), respectively, yields, after some manipulation,

$$y\frac{\partial q_0}{\partial y} + \Psi\nabla^2\tilde{\psi} + \tilde{\psi}f_0^2\frac{d}{dp}\left(\frac{1}{\sigma_r}\frac{d\Psi}{dp}\right) = \mathcal{F}(-U(p)y + \tilde{\psi}\Psi(p)). \quad (3.11)$$

To proceed beyond (3.11), it is necessary to determine the form of the function $\mathcal{F}$. Since we are looking for a localized structure, we require that the eddy decay to zero at infinity. For all streamlines that extend to infinity, it follows from (3.11) that the function $\mathcal{F}$ has the simple linear form

$$\mathcal{F}(*) \equiv [-(\partial q_0/\partial y)U^{-1}]*. \quad (3.12)$$

It therefore follows from (3.11) and (3.12) that

$$\Psi\nabla^2\tilde{\psi} + \tilde{\psi}f_0^2\frac{d}{dp}\left(\frac{1}{\sigma_r}\frac{d\Psi}{dp}\right) = \frac{dq_0}{d\psi_0}\Psi\tilde{\psi}, \quad (3.13)$$

for all those streamlines that extend to infinity, and where $dq_0/d\psi_0$ will be given by

$$\frac{dq_0}{d\psi_0} = \left[f_0^2\frac{d}{dp}\left(\frac{1}{\sigma_r}\frac{dU}{dp}\right) - \beta\right]\Big/U. \quad (3.14)$$

It is important to point out that in general $dq_0/d\psi_0$ is a function of pressure. Equation (3.13) can be rearranged into the form

$$\frac{\nabla^2\tilde{\psi}}{\tilde{\psi}} + \frac{f_0^2}{\Psi}\frac{d}{dp}\left(\frac{1}{\sigma_r}\frac{d\Psi}{dp}\right) - \frac{dq_0}{d\psi_0} = 0. \quad (3.15)$$

Letting $\gamma$ be the separation constant, we then obtain the following homogeneous Helmholtz equation,

$$\nabla^2\tilde{\psi} - \gamma\tilde{\psi} = 0, \quad (3.16)$$

for the horizontal problem, and

$$\frac{d}{dp}\left(\frac{1}{\sigma_r}\frac{d\Psi}{dp}\right) + f_0^{-2}(\gamma - \Lambda_0)\Psi = 0 \quad (3.17)$$

for the vertical problem, where

$$\Lambda_0(p) \equiv dq_0/d\psi_0 = -(\partial q_0/\partial y)U^{-1}. \quad (3.18)$$

As pointed out, in general, $\Lambda_0(p)$ is a function of pressure, or correspondingly a function of height. From our dataset we have estimated that the variation of $\Lambda_0$ is no more than about 25% from 500 mb to 700 mb or 400 mb. This is consistent with other findings. For example, Derome (1984) also finds that $\Lambda_0$ does not vary much with height. Thus, we shall assume that $\Lambda_0$ is a constant for the remainder of this paper.

The assumption that $\Lambda_0$ is a constant means that not every $U(p)$ is admissible. It follows from (3.14) that $U(p)$ will be determined by solving

$$f_0^2\frac{d}{dp}\left(\frac{1}{\sigma_r}\frac{dU}{dp}\right) - \Lambda_0 U = \beta, \quad (3.19)$$

subject to appropriate boundary conditions. In section 3c, we will give an analytical solution to (3.19) assuming a power law form for the static stability as estimated from our dataset.

For those streamlines that do not extend to infinity, there is no general procedure for determining the form of the function $\mathcal{F}(*)$. The modon model (e.g., Haines and Marshall 1987) assumes that $\mathcal{F}(*)$ is also a linear function of its argument (although with a constant of proportionality different than $\Lambda_0$). However, other choices are equally plausible, including highly nonlinear relationships. A more complete discussion of the possibilities can be found in Butchart et al. (1989). For our purposes in this paper it is not necessary to explicitly determine what form $\mathcal{F}(*)$ for those streamlines that do not extend to infinity.

### *c. The vertical mode problem and determination of the mean flow profile*

The vertical modes will satisfy (3.17), which must be supplemented with appropriate boundary condi-

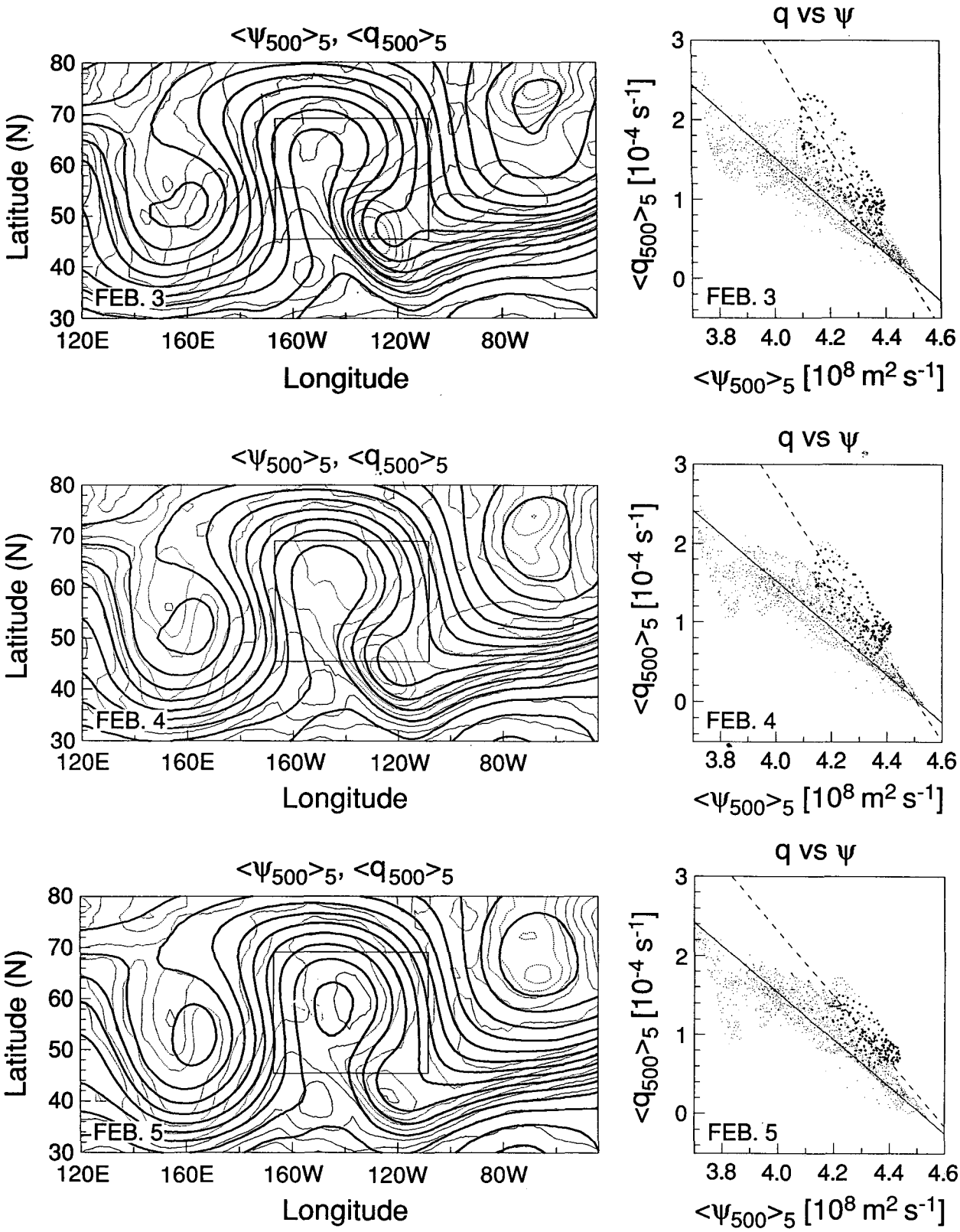


FIG. 4. Five-day mean 500-mb geostrophic streamfunction, $\psi$ (solid contours), and potential vorticity, $q$ (light dashed contours), with corresponding $q(\psi)$ scatter diagram. Contour intervals are $6 \times 10^6$ m$^2$ s$^{-2}$ for $\psi$ and $2 \times 10^{-5}$ s$^{-1}$ for $q$. Scatterplot crosses denote ($\psi$, $q$) values from within the box-shaped region in the middle of the contour chart. Small dots denote values from outside the same region. The dashed and solid lines on the scatterplots are the least-squares $q(\psi)$ lines for the interior and exterior regions, respectively: (a) 3 Feb 1989, (b) 4 Feb, (c) 5 Feb, (d) 16 Feb, (e) 17 Feb, (f) 18 Feb, (g) 19 Feb, (h) 20 Feb, (i) 21 Feb, and (j) 24 Feb.

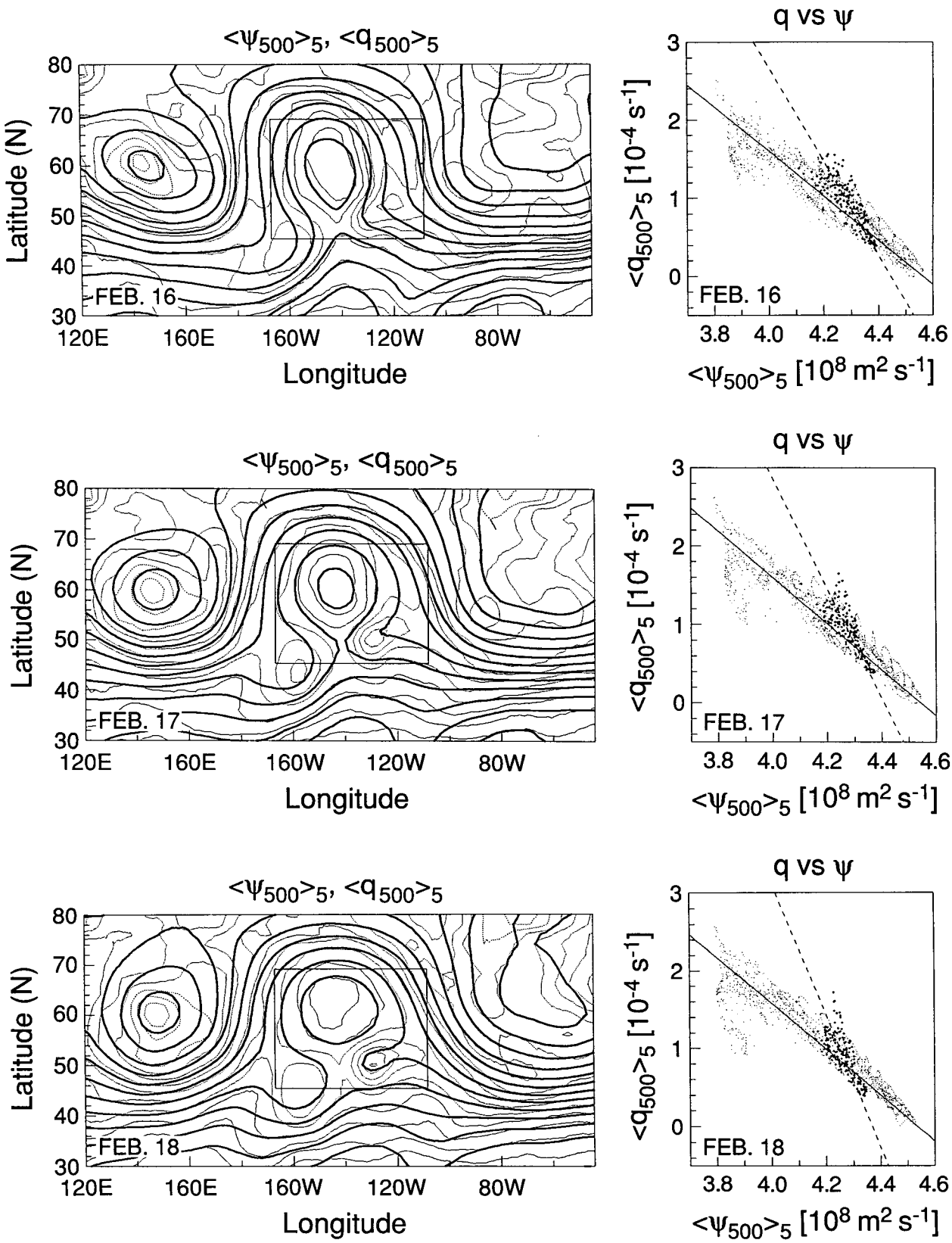


FIG. 4. (*Continued*)

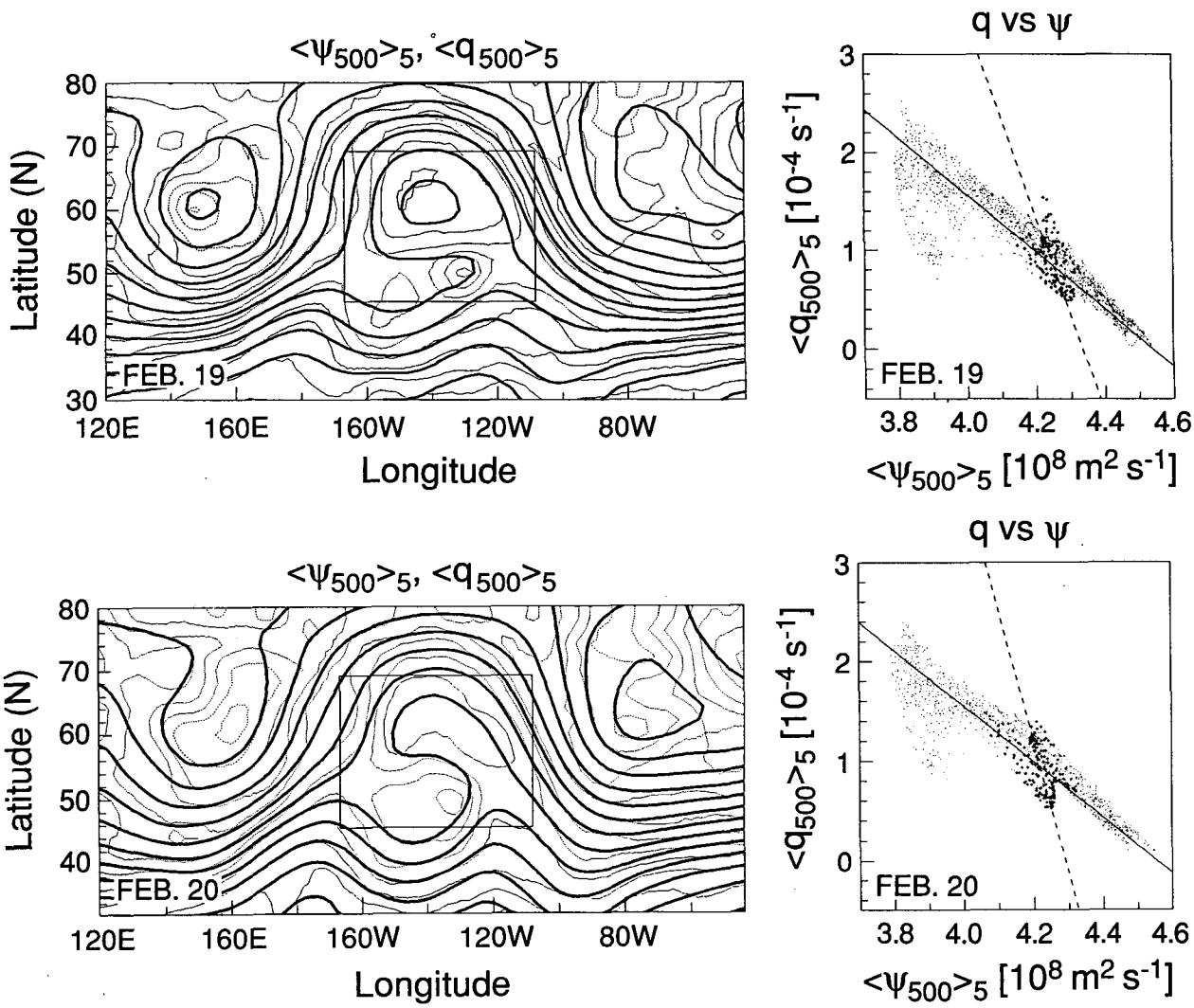


FIG. 4. (*Continued*)

tions. Both upper and lower boundaries are isobaric surfaces given by $p = p_t \equiv 250$ mb and $p = p_b = 850$ mb, respectively, on which we specify zero vertical velocity (i.e., $\omega \equiv Dp/Dt \equiv 0$). The steady, isentropic, quasigeostrophic thermodynamic equation then takes the form

$$J(\psi, \partial\psi/\partial p) = 0, \tag{3.20a}$$

on the upper and lower boundaries. Equation (3.20a) can be integrated immediately to imply

$$\partial\psi/\partial p = \tilde{f}(\psi), \tag{3.20b}$$

on $p = p_t$ and $p = p_b$; $\tilde{f}$ is determined by substituting for $\psi$ using (3.4a) and (3.9), and then invoking the far-field condition; namely, that the eddy component vanish as we go to infinity. This implies that for all those streamlines that extend to infinity

$$-(dU/dp)y = \tilde{f}(-U(p)y),$$

which in turn implies

$$\tilde{f}(*) = \frac{dU/dp}{U} *,$$

which when substituted into (3.20) yields

$$\frac{\partial\psi}{\partial p} = \frac{dU/dp}{U}\psi. \tag{3.21a}$$

Substitution of (3.4a), (3.6), and (3.9) into (3.21a) implies that the appropriate boundary conditions for the vertical modes is given by

$$\frac{d\Psi}{dp} - \frac{dU(p)/dp}{U(p)}\Psi = 0, \tag{3.21b}$$

on $p = p_t$ and $p = p_b$, respectively.

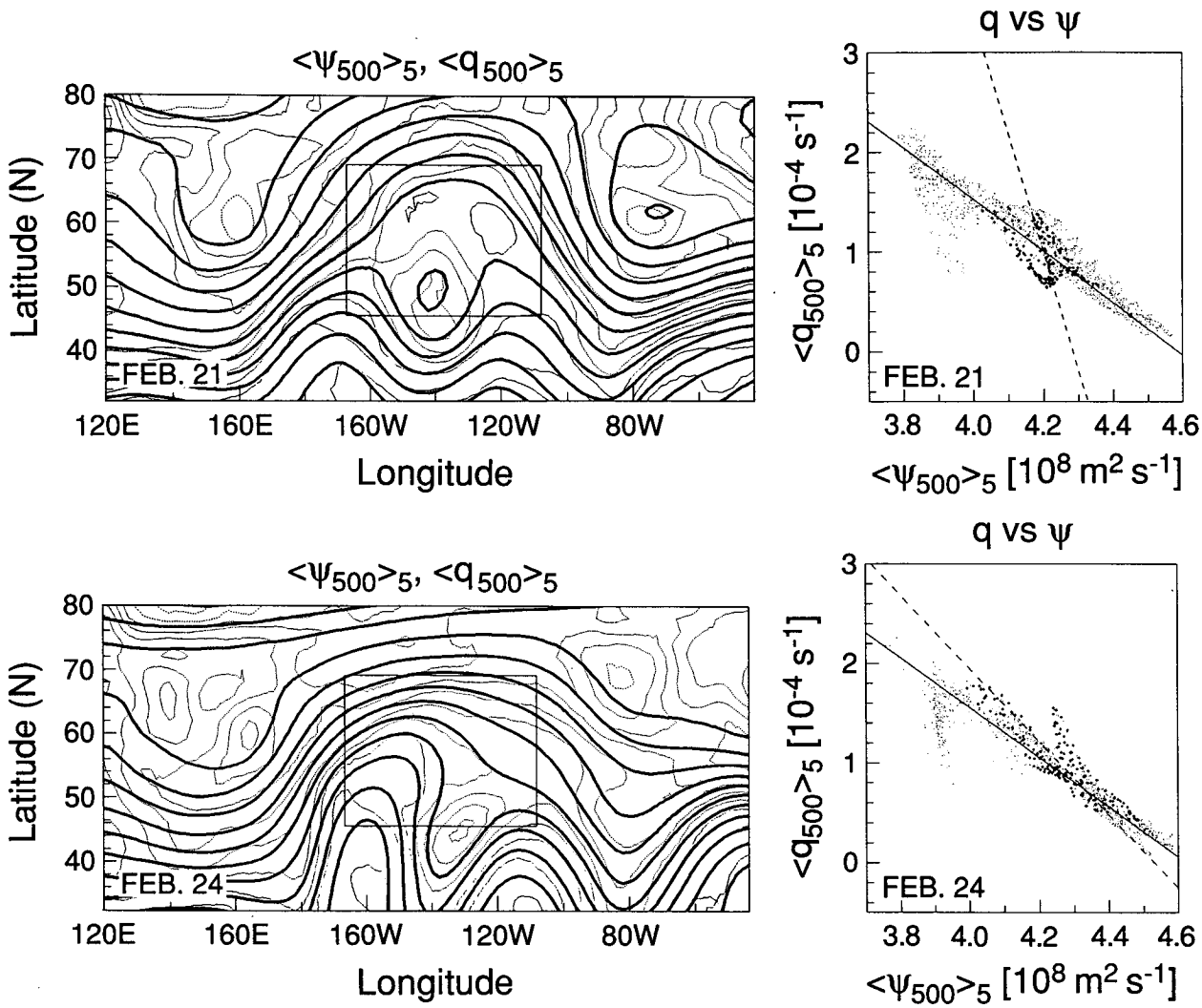


FIG. 4. (*Continued*)

Here again it is not possible, in general, to determine the form of the function $\hat{f}(*)$ on $p = p_t$ and $p_b$ for those streamlines that do not extend to infinity. In some oceanographic calculations of nonlinear eddy structures in a stratified flow (e.g., Hogg 1980; Swaters and Mysak 1985), it has been assumed that the boundary condition (3.21b) holds everywhere. Butchart et al. (1989) made a similar assumption.

Together, (3.17) and (3.21b) comprise a two-point Sturm–Liouville eigenvalue problem. For such problems, we are guaranteed an infinite sequence of $\gamma_n$, for $n = 0, 1, 2, \cdots$, such that $-\infty < \gamma_0 < \gamma_1 < \gamma_2 < \cdots$ (Zauderer 1989). It can also be shown (Butchart et al. 1989) that at least the minimum eigenvalue satisfies $\gamma_0 < 0$, for a westerly mean flow $U(p) > 0$. This means, in the context of stationary continuously stratified modon models for atmospheric blocks, the gravest mode will necessarily be radiating energy away from the block.

For completeness, we give an alternate demonstration of the Butchart et al. (1989) result using a Rayleigh–Ritz variational principle. If the transformation $\Psi(p) \equiv U(p)\Phi(p)$ is introduced into (3.17) and (3.21b), it follows that

$$f_0^2(U^2\Phi'/\sigma_r)' + (\gamma U^2 + \beta U)\Phi = 0,$$

$$\Phi' = 0, \quad \text{on} \quad p = p_t, p_b,$$

where $(\ )' \equiv d(\ )/dp$ and where we have used (3.19). If the differential equation for $\Phi$ is multiplied through by $\Phi$ and integrated over $p \in (p_t, p_b)$, it follows that

$$\gamma = \left\{ f_0^2 \int_{p_b}^{p_t} U^2(\Phi')^2/\sigma_r dp - \beta \int_{p_b}^{p_t} U\Phi^2 dp \right\} \Big/ \int_{p_b}^{p_t} U^2\Phi^2 dp.$$

Thus, a Rayleigh–Ritz variational principle for the minimum eigenvalue, denoted $\gamma_0$, is given by

$$\gamma_0 = \min_{\phi}\left[\left\{f_0^2\int_{p_b}^{p_t} U^2(\phi')^2/\sigma_r dp - \beta\int_{p_b}^{p_t} U\phi^2 dp\right\}\Big/ \int_{p_b}^{p_t} U^2\phi^2 dp\right],$$

where the minimization is carried out over all smooth (nontrivial) functions satisfying $\phi' = 0$ on $p = p_t$ and $p_b$, respectively. Clearly, one candidate is the constant $\phi \equiv 1$, so that we can bound $\gamma_0$ by

$$\gamma_0 \leq -\beta\int_{p_b}^{p_t} U(p)dp \Big/ \int_{p_b}^{p_t} U^2(p)dp,$$

from which we conclude $\gamma_0 < 0$ if $U(p) > 0$ for all $p \in (p_t, p_b)$. The implications of this result will be commented on momentarily.

To make any further analytical progress, we have to settle on an equation for the static stability $\sigma_r(p)$. Below the tropopause, and neglecting the planetary boundary layer, $\sigma_r$ can be reasonably well approximated by a power law,

$$\sigma_r \approx Ap^b. \tag{3.22}$$

Holton (1979) points out that $b = -2$ is exactly equivalent to an isothermal atmosphere. It is possible to give a simple physical justification for the power law (3.22). For a hydrostatic atmosphere in which the reference lapse rate $\Gamma \equiv -dT_r/dz$ is approximately constant, it is straightforward to show that

$$\sigma_r = \left[\frac{1}{c_p} - \frac{\Gamma}{g}\right]\frac{R^2\theta_*}{p_0^{R/c_p}} p^{-2+R/c_p} \tag{3.23}$$

(Holton 1979), where we have also assumed that the reference potential temperature $\theta_*$ in (3.23) is approximately constant (essentially a Boussinesq approximation).

Substituting for $\sigma_r$ in (3.17) using the power law (3.22), we can write our vertical mode equation as

$$\frac{d}{dp}\left[p^{-b}\frac{d\Psi}{dp}\right] + \frac{Ak^2}{f_0^2}\Psi = 0, \tag{3.24}$$

where $k^2 \equiv \gamma - dq_0/d\psi_0$ with $dq_0/d\psi_0$ now assumed constant, and with the boundary conditions (3.21b). It turns out that this equation is one of the many varied forms of Bessel's equation (Hildebrand 1976). The independent solutions can be written in the form

$$p^{(1+b)/2} Z_{(1+b/2+b)}\left(\frac{\sqrt{A}k}{f_0}\frac{1}{b/2+1}p^{1+b/2}\right), \tag{3.25}$$

where $Z_\nu$ is an ordinary Bessel function of either the first or second kind, of order $\nu$. In our case, the exponent $b$ in (3.22) is

$$b \equiv -2 + R/c_p \equiv -2 + \epsilon \approx -1.714,$$

so that the index is

$$\nu \equiv 1 - 1/\epsilon \approx -2.501,$$

and our general solution to (3.24) is therefore

$$\Psi(p) = p^{(\epsilon-1)/2}\left[c_1 J_{1/\epsilon-1}\left(\frac{2k\sqrt{A}}{\epsilon f_0}p^{\epsilon/2}\right) + c_2 J_{1-1/\epsilon}\left(\frac{2k\sqrt{A}}{\epsilon f_0}p^{\epsilon/2}\right)\right]. \tag{3.26}$$

The functions $J_{1/\epsilon-1}$ and $J_{1-1/\epsilon}$ are the (linearly independent) Bessel functions of order $\pm(1 - 1/\epsilon)$ of the first kind. The constants $c_1$ and $c_2$ are undetermined at this point. The parameter $\epsilon$ can be interpreted as a measure of the degree to which the reference hydrostatic atmosphere is not isothermal.

Substitution of (3.26) into the boundary condition (3.21) evaluated for the lower boundary $p = p_b$ yields, after some algebra,

$$c_1\left[-\frac{\epsilon}{2}\alpha_b k J_{1/\epsilon-2}(\alpha_b k) + \left(1 - \epsilon + p_b\frac{U'(p_b)}{U(p_b)}\right)J_{1/\epsilon-1}(\alpha_b k)\right] + c_2\left[\frac{\epsilon}{2}\alpha_b k J_{2-1/\epsilon}(\alpha_b k) + \left(1 - \epsilon + p_b\frac{U'(p_b)}{U(p_b)}\right) \times J_{1-1/\epsilon}(\alpha_b k)\right] = 0, \tag{3.27a}$$

where

$$\alpha_b \equiv \frac{2\sqrt{A}}{\epsilon f_0}p_b^{\epsilon/2}.$$

Similarly for the upper boundary $p = p_t$, one obtains

$$c_1\left[-\frac{\epsilon}{2}\alpha_t k J_{1/\epsilon-2}(\alpha_t k) + \left(1 - \epsilon + p_t\frac{U'(p_t)}{U(p_t)}\right)J_{1/\epsilon-1}(\alpha_t k)\right] + c_2\left[\frac{\epsilon}{2}\alpha_t k J_{2-1/\epsilon}(\alpha_t k) + \left(1 - \epsilon + p_t\frac{U'(p_t)}{U(p_t)}\right) \times J_{1-1/\epsilon}(\alpha_t k)\right] = 0, \tag{3.27b}$$

where

$$\alpha_t \equiv \frac{2\sqrt{A}}{\epsilon f_0} p_t^{\epsilon/2}.$$

This pair of equations, (3.27a) and (3.27b), has nontrivial solutions if and only if the determinant of the coefficient matrix associated with $c_1$ and $c_2$ is zero, which can be written in the form

$$\begin{aligned}
&\left[\frac{\epsilon}{2}\alpha_b k J_{1/\epsilon-2}(\alpha_b k)\right. \\
&\left. - \left(1 - \epsilon + p_b \frac{U'(p_b)}{U(p_b)}\right) J_{1/\epsilon-1}(\alpha_b k)\right] \\
&\times \left[\frac{\epsilon}{2}\alpha_t k J_{2-1/\epsilon}(\alpha_t k)\right. \\
&\left. + \left(1 - \epsilon + p_t \frac{U'(p_t)}{U(p_t)}\right) J_{1-1/\epsilon}(\alpha_t k)\right] \\
&- \left[\frac{\epsilon}{2}\alpha_b k J_{2-1/\epsilon}(\alpha_b k)\right. \\
&\left. + \left(1 - \epsilon + p_b \frac{U'(p_b)}{U(p_b)}\right) J_{1-1/\epsilon}(\alpha_b k)\right] \\
&\times \left[\frac{\epsilon}{2}\alpha_t k J_{1/\epsilon-2}(\alpha_t k)\right. \\
&\left. - \left(1 - \epsilon + p_t \frac{U'(p_t)}{U(p_t)}\right) J_{1/\epsilon-1}(\alpha_t k)\right] = 0.
\end{aligned} \tag{3.28}$$

This equation determines the eigenvalue $k$ (and thus $\gamma$) as a function of the other parameters.

Employing the same assumptions for the form of the static stability $\sigma_r$ given by (3.22) and for $\Lambda_0$ (i.e., constant), the general solution for $U(p)$ as determined by (3.19) can be written in the form

$$\begin{aligned}
U(p) = p^{(\epsilon-1)/2}&\left[h_1 J_{1/\epsilon-1}\left(\frac{2\sqrt{-A\Lambda_0}}{\epsilon f_0} p^{\epsilon/2}\right)\right. \\
&\left. + h_2 J_{1-(1/\epsilon)}\left(\frac{2\sqrt{-A\Lambda_0}}{\epsilon f_0} p^{\epsilon/2}\right)\right] - \frac{\beta}{\Lambda_0}.
\end{aligned} \tag{3.29}$$

We solve for the constants $h_1$ and $h_2$ by specifying $U$ at the upper and lower boundaries. Then we calculate analytically the boundary values of $U'(p)/U(p)$ needed for (3.28). We emphasize, as shown by Butchart et al. (1989) and above that this procedure guarantees that the gravest eigenvalue for the *horizontal* boundary value problem (3.16) is negative. This means that the gravest-mode horizontal solution to (3.16), in the context of our analysis, is not isolated in the sense that the area-integrated energy and enstrophy is finite; Rossby wave–type solutions are possible. This does not discount the possible existence of modonlike solutions, though, because as Haines and Marshall (1987) have demonstrated, modonlike structures can still exist in the presence of Rossby wave radiation, for time scales comparable to typical atmospheric blocking durations. The vertical eigenfunctions and mean flow wind profile as computed using our data are shown in Figs. 7 and 8, respectively (also see the discussion in section 4a and 4d).

### *d. Scatter diagrams and free modes*

A means of testing the applicability of free modes to blocking originates with an interesting result of Read et al. (1986). Suppose that we pick an arbitrary, simple horizontal curve enclosing a region $\mathcal{R}_{(x,y)}$, in physical $(x, y)$ space. The net flux of vorticity across the curve, $\partial\mathcal{R}_{(x,y)}$, due to the geostrophic wind, can be written as

$$F_q \equiv \oint_{\partial\mathcal{R}_{(x,y)}} q\mathbf{v}_g \cdot \mathbf{n} dl, \tag{3.30}$$

where $\mathbf{v}_g \equiv \mathbf{k} \times \nabla\psi$ is the geostrophic wind, $\mathbf{n}$ is the outward unit normal vector to the curve $\partial\mathcal{R}_{(x,y)}$, $dl$ is the differential arc length, $\mathbf{k}$ is the unit vector pointing vertically upward, and $\nabla = (\partial/\partial x, \partial/\partial y)$.

A positive flux entails a net export of cyclonic vorticity. We can apply the two-dimensional divergence theorem to (3.30) to get

$$\begin{aligned}
F_q &= \iint_{\mathcal{R}_{(x,y)}} \nabla\cdot[q(\mathbf{k} \times \nabla\psi)] dxdy \\
&= \iint_{\mathcal{R}_{(x,y)}} J(\psi, q) dxdy.
\end{aligned} \tag{3.31}$$

The second integral in (3.31) may be directly transformed into an integral over the corresponding region $\tilde{\mathcal{R}}_{(\psi,q)}$, in $(\psi, q)$ space as follows:

$$\begin{aligned}
F_q &= \iint_{\mathcal{R}_{(x,y)}} \mathrm{sgn}[J(\psi, q)]\,|J(\psi, q)|\, dxdy, \\
&= \iint_{\tilde{\mathcal{R}}_{(\psi,q)}} \mathrm{sgn}[J(\psi, q)] d\psi dq.
\end{aligned} \tag{3.32a}$$

The sign of the Jacobian is positive if the curve in $(\psi, q)$ space is closed off in the same sense as the corresponding $(x, y)$ space curve, which we take to be counterclockwise. The sign is negative for $(\psi, q)$ curves that are closed off in the clockwise sense. Alternatively, we can relate the area of the $q/\psi$ scatter diagram, denoted by $A_{(\psi,q)}$, to the Jacobian as follows:

$$A_{(\psi,q)} \equiv \iint_{\tilde{\mathcal{R}}_{(\psi,q)}} d\psi dq$$

$$= \iint_{\mathcal{R}_{(x,y)}} |J(\psi, q)|\, dxdy. \quad (3.32b)$$

In the case of a free mode formally defined by $q = q(\psi)$, we have $J(\psi, q) = 0$, and both the area of the $(\psi, q)$ region, and $F_q$, must vanish. It is evident that either of the two quantities, $F_q$ or $A_{(\psi,q)}$, may be thought of as a measure of the *departure* of the system from *any* free mode of the form $q = q(\psi)$.

Because the computation of the $(\psi, q)$ space integral in (3.32), using actual data, is difficult, Read et al. (1986) proposed the use of

$$I \equiv \frac{\text{area enclosed on the } q(\psi) \text{ plot}}{\text{area of the circumscribing rectangle}},$$

as a measure of the degree to which the system departed from a free-mode form. Calculating the quantity $I$, however, is also a nontrivial task. The area of the circumscribing rectangle can vary, depending on its orientation. Choosing the proper orientation for the rectangle is in turn difficult because the slope of the scatterplot changes over time.

We have computed the line integral in (3.30) via a modified procedure using finite differences along the edges of the fixed box-shaped region shown in Fig. 2. The $(\psi, q)$ space area integral in (3.32a) was computed using the following technique. Although (3.30) expresses the net vorticity flux as a *single* line integral around the outer boundary of our fixed region, we can obtain the same result by evaluating (3.30) around *individual* grid boxes and then summing over all the grid boxes within the block region. The contributions from adjacent interior grid-box edges then cancel, leaving only the contributions from the outside edges. It is thus possible to calculate the area enclosed by the $(\psi, q)$ curve, corresponding to this outside edge, as the sum of the areas corresponding to all the individual grid boxes within the block region. The $(\psi, q)$ curve corresponding to *each individual* grid box encloses an area, denoted $\delta A_{(\psi,q)}$, that can be computed using integrals of the form

$$\delta A_{(\psi,q)} = \frac{1}{2} \oint [\psi dq - q d\psi]. \quad (3.33)$$

This expression, together with (3.32a,b), implies that the net vorticity flux and $q/\psi$ scatter diagram area can be computed as, respectively,

$$F_q \approx \sum \text{sgn}[J(\psi, q)]\delta A_{(\psi,q)}, \quad (3.34a)$$

$$A_{(\psi,q)} = \sum \delta A_{(\psi,q)}, \quad (3.34b)$$

where the sum is understood to be over all *individual* grid boxes and a constant sign for the Jacobian is assumed for each individual $\delta A_{(\psi,q)}$ in (3.34a).

## 4. Application to the Pacific block of February 1989

### a. Estimating various parameters

#### 1) LEAST-SQUARES SLOPE OF $q(\psi)$ SCATTERPLOTS

Because a latitude–longitude grid has been used, simply using $(\psi, q)$ values from all grid points would give far too much emphasis to the northern regions in our dataset, where grid points are closer together in the zonal direction. Hence for the calculations of the least-squares fit $q(\psi)$ lines, the $(\psi, q)$ values are interpolated linearly in the zonal direction, at a constant zonal spacing of 192 km (the zonal grid spacing at 30°N). In this way the lines are computed using $(\psi, q)$ values taken from roughly equidistant points on the 500-mb surface.

Our use of the fixed box-shaped approximation to the block entails that some $(\psi, q)$ values will be counted as "interior" values, when in fact they are from outside the block. In order to decrease this contamination of the interior least-squares line by the inevitable inclusion of exterior $(\psi, q)$ values, we have excluded from the interior least-squares calculation those $(\psi, q)$ values for which the value of $\psi$ lies more than 1.8 standard deviations from the mean $\psi$ value within the box.

We estimate our constant value of $\Lambda_0 \equiv dq_0/d\psi_0$ by computing the average, over 35 days (23 January through 26 February), of the least-squares slope from the exterior region, at 500 mb. The value thus obtained was $\Lambda_0 \approx -2.87 \times 10^{-12}\ \text{m}^{-2}\ \text{s}^{-2}$.

#### 2) CONSTANTS IN THE VERTICAL NORMAL-MODE SOLUTION

The coefficient $A$ in the static stability power law (3.22) was estimated using (3.23), in which in turn estimates for $\Gamma$ and $\theta_r$ are also required. From the dataset, the virtual potential temperature averaged over the entire layer 850 to 250 mb, over all days, was approximately 300 K. The lapse rate, $\Gamma$, was initially estimated using centered differences between each data level of the daily area mean (reference) virtual temperature, $T_r$; that is,

$$\Gamma = -\frac{dT_r}{dz} = \frac{gp}{RT_r}\frac{dT_r}{dp},$$

in which the hydrostatic equation and the gas law have also been applied. A weighted average of $\Gamma$ was then computed over the interval 850 to 250 mb, and averaged over all days. The resulting constant lapse rate was found to be approximately

$$\Gamma \approx 5.23°\text{C/km}.$$

We work within the range $5.23°\text{C/km} \leq \Gamma \leq 7.42°\text{C/km}$ (roughly centered about the *U.S. Standard Atmosphere* lapse rate of 6.5°C/km). The corresponding range in the parameter $A$ is given by $219.5 \leq A \leq 426.1$.

TABLE 1. Computed values of $U'(p)/U(p)$ at $p = p_b$ and $p_t$.

| | $U'(p)/U(p)$ ($\times 10^{-5}$ Pa$^{-1}$) | |
|---|---|---|
| $A$ | $p$ = 850 mb | $p$ = 250 mb |
| 426.1 | −2.88 | −1.43 |
| 219.5 | −2.28 | −2.63 |

TABLE 2. Computed vertical normal-mode eigenvalues.

| $n$ | $k_n$ ($\times 10^{-6}$ m$^{-1}$) |
|---|---|
| 0 | 1.31/1.38 |
| 1 | 5.36/4.08 |
| 2 | 9.66/10.51 |
| 3 | 14.46/13.80 |

The term $U'(p)/U(p)$ in (3.28) was computed from our solution (3.29) as follows. The estimated zonal winds at 850 mb and 250 mb were first computed as the geostrophic winds at those levels, zonally averaged along latitudes 46°N and 70°N, but excluding values from inside our box (between longitudes 114°W and 166°W). The average values over all 35 days (from 23 January through 26 February) were approximately 4.17 and 16.7 m s$^{-1}$, respectively. We then determined the constants $h_1$ and $h_2$ in (3.29) and computed analytically the values for $U'(p)/U(p)$ at 850 mb and 250 mb, respectively. For comparison we computed two pairs of values, one corresponding to $A$ = 426.1, the other to $A$ = 219.5. The approximate values of $U'(p)/U(p)$ so obtained are listed in Table 1.

We remark that the profile $U(p)$ we obtained matches quite well with our estimates of the zonal flow at 700, 500, and 400 mb; see section 4d.

The eigenvalues $k_n$ were obtained by numerically solving (3.28). The first four eigenvalues thus found are listed in Table 2. The two numbers given in each row of the table are the values found with $A$ = 219.5 and $A$ = 426.1 ($\Gamma$ = 7.42°C km$^{-1}$ and $\Gamma$ = 5.23°C km$^{-1}$), respectively. Examination of (3.22) and (3.25) shows that the magnitude of the eigenvalues is closely related to the value of $A$, which in turn is rather sensitive to the constant lapse rate $\Gamma$. We have used the $k_n \equiv (\gamma_n - \Lambda_0)^{1/2}$, corresponding to $A$ = 219.5, for the vertical structure computations. Numerical experiments showed that this choice had no discernible effect on any of the results.

### b. *Scatter diagrams*

The streamfunction–vorticity scatter diagram is relatively simple to construct. Values of $q$ at many grid points are plotted against the corresponding values of $\psi$. To see whether the $q(\psi)$ relations for the exterior and interior regions differ, as they do for the modon, we plot ($\psi$, $q$) values from within the block using a different symbol than that used for values from the exterior (see Fig. 4).

Using the smoothed fields, the series of scatterplots was constructed by plotting for each day absolute vorticity ($\zeta_a$) as well as potential vorticity ($q$) against $\psi$ for grid points of approximately equal geographical spacing. For the plots in Fig. 4, a simple spacing algorithm has been employed that picks out grid points that are spaced approximately equally, along each grid row (in the zonal direction). Every point whose values are plotted represents the center of a grid square, with a geographical area equal to approximately 49 000 km$^2$.

In general there were few differences between the 500-mb diagrams and those of the other pressure levels. This weak vertical variation is confirmed by our analysis of the vertical normal modes. The scatter plots using *absolute* vorticity ($\psi$ vs $\zeta_a$) are quite similar to the $\psi$ versus $q$ plots; Fig. 5 shows the $\zeta_a(\psi)$ plot for 19 February. One interesting observation is that our 500-mb level scatter charts show the least scatter; also, during the dipole stage, the linear, multivalued $q(\psi)$ relationship at this level is the most "modonlike." This contrasts somewhat with the results of Butchart et al. (1989). They derived most of their conclusions from charts at the 300-mb level and observed that the 500-mb *absolute* vorticity scatterplots seemed to be more modonlike.

As the Arctic disturbance intensifies and moves southeastward during the last days of January, the scatterplots steepen slightly. There emerges a distinct "lobe" of interior points on the scatter diagrams, easily

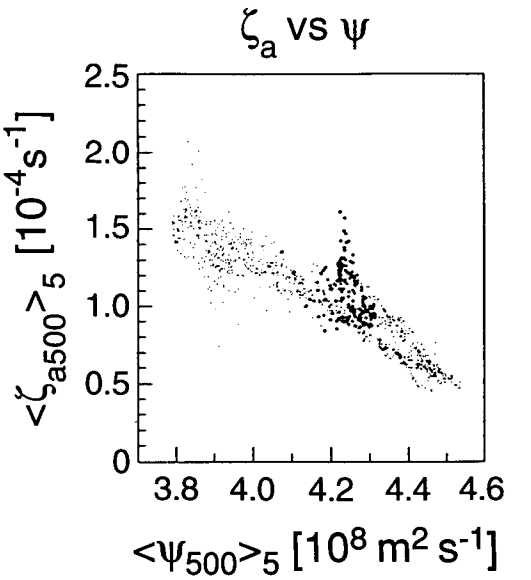


FIG. 5. Scatterplot of five-day mean 500-mb geostrophic streamfunction, $\psi$, versus vertical component of absolute vorticity, $\zeta_a$, for 19 February. Crosses and dots have the same meaning as in Fig. 4.

discernible on 3 February (Fig. 4a). This cluster of points is clearly due to the disturbance, since it is composed of relatively low streamfunction, high vorticity values. With time, the lobe moves toward higher streamfunction and lower vorticity, consistent with the translation of the vortex southeastward. Although we see a multivalued vorticity–streamfunction relation for the week ending on about 4 February (see Figs. 4a,b), it is clear that the streamfunction and vorticity fields are not those of a dipole. This indicates that a nonanalytic, linear $q(\psi)$ relation may not be sufficient for the flow to have the modon free-mode form. The disturbance clearly does not seem to have zero net angular momentum, which is a requirement for a persistent (quasi-stationary) isolated beta-plane eddy (Stern 1975; Flierl et al. 1983), and thus we would expect it to translate.

The initial steepening due to the arctic disturbance is consistent with the observations of Malanotte-Rizzoli and Hancock (1987). For their composite of 12 North Atlantic blocking ridges, they describe, in their terminology, a northern barrier of the trapping potential, which emerges and intensifies during the first week. This is equivalent to a steepening of the $q(\psi)$ scatterplot. It is interesting that in their study, as in ours, the source of the initial steepening is from the north.

Hansen and Chen (1982) have observed that blocking can be initiated by intense synoptic-scale activity, in which nonlinear, upscale energy transfer from synoptic systems contributes to block formation. It could be that the February 1989 block is also initiated by the intense arctic cyclonic disturbance preceding it. If this is so, it leads to the fascinating concept of identifying synoptic-scale disturbances that are capable of initiating a block, by monitoring scatterplots of the 5-day mean streamfunction versus potential vorticity.

Of equal significance is the means by which the block dissipates. This event seems to be accompanied by another less intense cyclonic disturbance that develops out of the cyclonic component of the dipole block, and then moves southeastward away from the block region after 24 February (see Fig. 4j). This process is also accompanied by a steepening of the scatterplots. However, this system and the associated steepening of the scatterplots are not as strong as for the intense arctic system preceding the block.

### c. *Vorticity flux and the area of the $q(\psi)$ plots*

In Fig. 6 we present time series of the computed net vorticity flux using the Cartesian representation (3.30) and the $q-\psi$ scatter diagram area representation (3.34a), respectively. The two quantities are in quite good agreement, as they should be, from which we conclude that it is possible to calculate the net vorticity flux using either representation as suggested by Read et al. (1986), and that our data are reasonably consistent. Repeating the calculations using a slightly larger box (Ek 1992) produces nearly identical results, suggesting that the sensitivity to our choice of boundary, in this case, is not too severe.

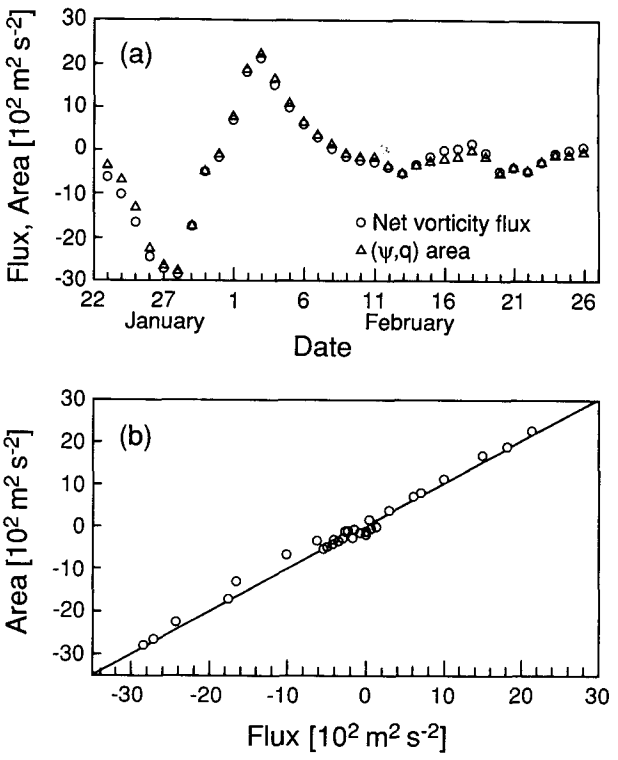


FIG. 6. (a) Time series of the area of the 500-mb net vorticity flux across the box bounded by latitudes 46°–70°N and longitudes 114°–166°W as computed directly from Cartesian coordinate and $q/\psi$ scatter diagram representations, respectively. The area values are computed using ($\psi$, $q$) values from inside the box, as well as along the edges. (b) The same variables as (a): net vorticity flux calculation in Cartesian coordinates plotted against the $q/\psi$ scatter diagram calculation.

The time series of the net flux clearly shows that it remains near zero values for the lifetime of the block. This suggests that the block is very near to an inertial free mode of the quasigeostrophic equations in the geostationary reference frame. The vorticity flux time series does not seem to distinguish between the different blocking configurations.

The net flux evolves in a manner that we can relate to the development of the block. Between 23 and 28 January, the net flux becomes more negative, which is consistent with the advection of cyclonic vorticity into the block region by the intense arctic disturbance. As that system moves through and exits the rectangular region, the net flux increases strongly, up to 3 February. This is interpreted as a loss of cyclonic vorticity from the region, which is consistent with the amplification of the (anticyclonic) blocking ridge during the first week in February.

Between 3 and 8 February, the net flux decreases, and after 8 February it remains near zero; during this

time the Omega block persists over the northeast Pacific, until the emergence of the dipole configuration between 18 and 21 February. The flux is slightly negative during the dipole period, indicating a net import of cyclonic vorticity into the block region. This may help to explain the breakdown of the anticyclonic component of the dipole after 21 February. The cyclonic vortex that drifts southeastward out of the block region does not appear to be associated with any significant change in the net flux. Therefore, even though this vortex may play a key role in the breakdown of the block, the physical mechanism at work could be different from that of the intense arctic disturbance preceding the block. It may be that the capability of the two intense vortices to generate or dissipate the block can be identified in advance by both the steepening of the scatterplot *and* the sustained increase in net vorticity flux.

### *d. The normal modes*

#### 1) VERTICAL EIGENFUNCTIONS

The eigenfunctions $\Psi_n(p)$, $n = 0, 1, 2, 3$, are computed using the solution (3.26), which, with $\epsilon \equiv R/c_p \approx 2/7$, takes the form

$$\Psi_n(p) = p^{-5/14}\left[ c_{1,n}J_{5/2}\left(\frac{7\sqrt{A}k_n}{f_0}p^{1/7}\right) + c_{2,n}J_{-5/2}\left(\frac{7\sqrt{A}k_n}{f_0}p^{1/7}\right)\right]. \quad (4.1)$$

We let $c_{1,n} = -1$, and $c_{2,n}$ is defined by the upper boundary condition (3.27b). The eigenfunctions were orthonormalized over the interval $[p_b, p_t]$, using the Gram–Schmidt procedure as described in Arfken (1985), so that they satisfy the relation

$$\frac{1}{(p_b - p_t)}\int_{p_t}^{p_b} \Psi_m(p)\Psi_n(p)dp = \delta_{mn} \quad (4.2)$$

and are depicted in Fig. 7. The solution for the mean zonal wind is depicted in Fig. 8.

We used the orthonormalized eigenfunctions as the basis functions in a generalized spectral expansion for the vertical structure of the *eddy* streamfunction, within the same fixed box that approximates the region occupied by the block. The eddy streamfunction is defined from (3.4a) as

$$\psi_1(x, y, p) = \psi(x, y, p) - \psi_r(p) - \psi_0(y, p),$$

where $\psi(x, y, p)$ was approximated by the 5-day-averaged data, and $\psi_r$ is a hydrostatic reference streamfunction. We used the constant lapse rate 5.23°C/km to calculate a reference thermal profile, which was then used with the gas law and the hydrostatic equation to

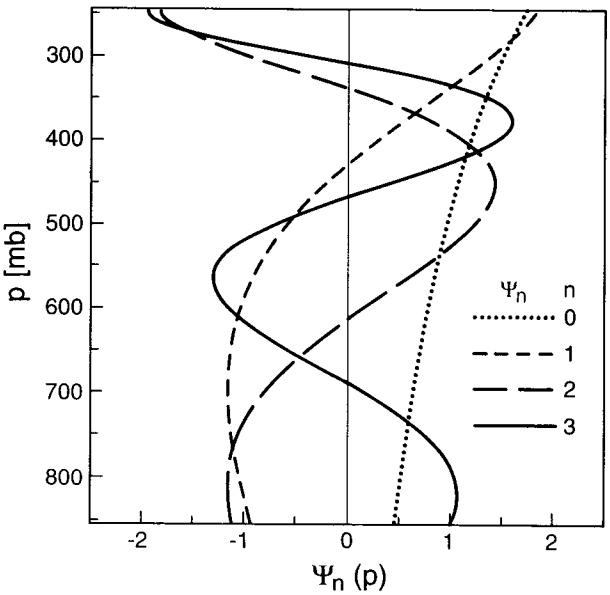


FIG. 7. The vertical modes $n = 0$, 1, 2, and 3. These are the solutions to the boundary-value problem (3.19) and (3.21).

compute values of $\psi_r$ at each data level (850, 700, 500, 400, and 250 mb). We estimated the zonal flow

$$\psi_0 = -U(p)y,$$

by using our solution $U(p)$ given by (3.29), and computing $y$ as the distance along longitude lines from 30°N. After subtracting out the reference and zonal flow components, we were left with estimates of the eddy streamfunction that are evenly spaced horizontally, at five data levels. We then interpolated linearly in the vertical, at 60 equidistant levels between 850 and 250 mb.

The spectral decomposition of the eddy fields onto the normal modes is given by

$$\psi_1(x, y, p) = \sum_{n=0}^{\infty} a_n(x, y)\Psi_n(p).$$

We calculated the four lowest terms in the series, at each point $(x, y)$. The normal-mode coefficient functions $a_0$, $a_1$, $a_2$, and $a_3$ were computed using

$$a_n(x, y) = \frac{1}{(p_b - p_t)}\int_{p_t}^{p_b} \psi_1(x, y, p)\Psi_n(p)dp. \quad (4.3)$$

The integrals in (4.2) and (4.3) were evaluated by Simpson's method, using interpolated values at the 60 equidistant pressure levels between 850 and 250 mb.

For each day, one set of four coefficients was thus calculated for each evenly spaced grid point within the block region. There are 204 such points, at each of the five data levels. In order to be able to compare the average contribution of each mode to the vertical struc-

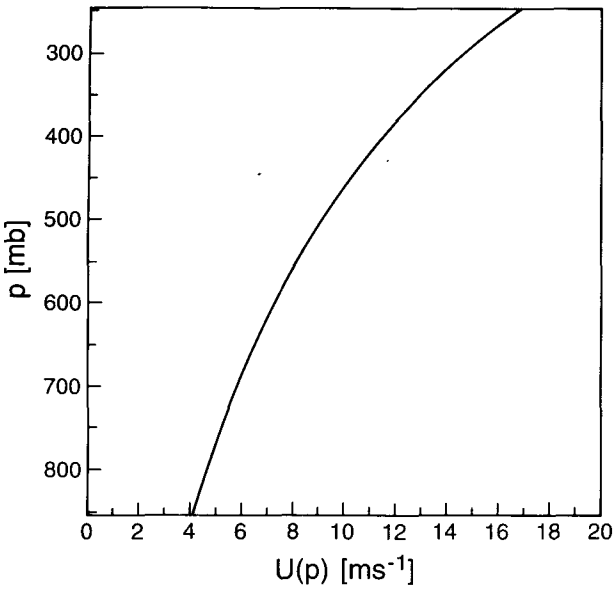


FIG. 8. The vertical structure of the mean wind profile.

ture of the blocking eddy, we computed the root-mean-square (rms) value of each coefficient, defined as

$$\langle a_n \rangle_{\text{rms}} = \left[ \sum_{x,y}^{(N \text{ points})} \frac{[a_n(x, y)]^2}{N} \right]^{1/2}.$$

For each day, the rms values were then scaled so that the sum of their squares is unity. The foregoing computations were repeated for each day from 23 January through 26 February.

### 2) THE BAROCLINICITY OF THE BLOCK

The similarity of the 500-mb absolute and potential vorticity scatter diagrams has been mentioned. This similarity indicates that the block is not too far from being equivalent barotropic, for the space and time scales with which we are concerned. We examine this question in more detail using our quasigeostrophic vertical normal modes. The time series of the normalized root-mean-square (rms) normal-mode coefficients is shown in Fig. 9. The magnitude of each normalized coefficient shows the relative contribution of its mode to the total vertical structure of the eddy component of the streamfunction.

The contribution of the gravest, "quasi-barotropic" mode (see Fig. 9a) appears to dominate the other modes during the entire series, confirming that the block is nearly equivalent barotropic. During the first week in February, when the block first forms, there is a small but definite increase in the contribution of the gravest mode, matched by a decrease in the contributions of the higher baroclinic modes. For the duration of the block, the contribution of the gravest mode is practically constant.

Examining the contoured streamfunction and potential vorticity charts for 16 through 19 February reveals a fairly intense cyclonic vortex that has developed within the block region, southeast of the cutoff anticyclone (see Figs. 4d–g). A second, weaker vortex lies southwest of the anticyclone. The merging of the two vortices, south of the anticyclone, results in the dipole on 20 February.

We suggest that the vortices entrained into the block, thereby forming the dipole, may play a role similar to the synoptic-scale eddies observed by Illari (1984) and Shutts (1986), which force the dipole to form. In the eddy-straining process, however, the eddies are baroclinically inactive (Haines and Marshall 1987), while our vertical normal mode analysis seems to indicate that, immediately preceding the formation of the dipole, there is a brief period of slightly increased baroclinic activity. This does not seem to be associated with any significant change in the net vorticity flux. The fact that it is a *brief* episode of synoptic-scale activity suggests that the same nonlinear, upscale energy transfer observed by Hansen and Chen (1982) may be acting in this instance.

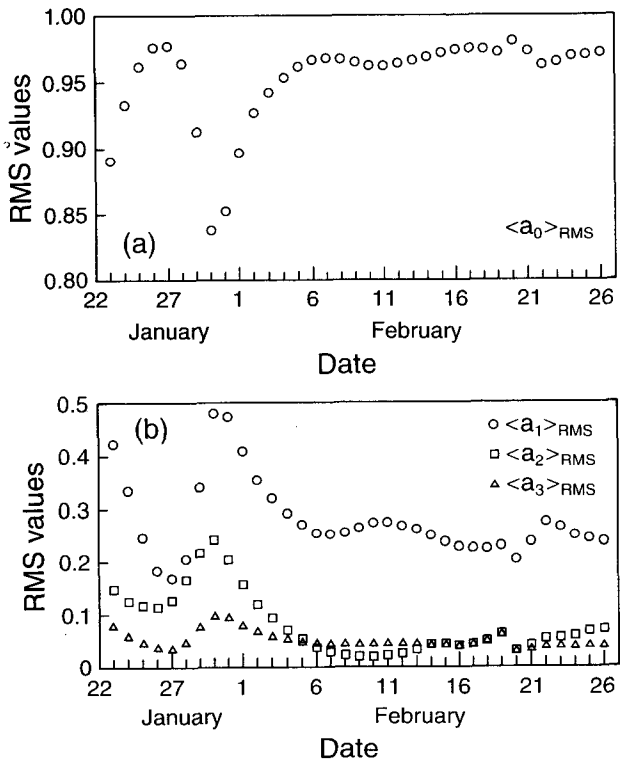


FIG. 9. Time series of normalized root-mean-square (rms) Fourier coefficients of the four gravest vertical normal modes. The region over which the rms is computed is the box shape bounded by latitudes 46°–70°N and longitudes 114°–166°W: (a) gravest mode; (b) first, second, and third modes. Normalizations are such that the sum of the squares of each day's four rms values is unity.

*e. Block stability*

Throughout our time series, $dq/d\psi$ and $d\zeta_a/d\psi$ are seen to be always negative. We can qualitatively relate this to a tendency toward or away from the possibility of hydrodynamic stability, by utilizing Arnol'd's second linear Liapunov stability theorem for nonparallel flows (Arnol'd 1966; McIntyre and Shepherd 1987). The theorem states that a sufficient condition for the linear stability of a quasigeostrophic steady flow described formally by $q = q(\psi)$, in a domain $\mathbb{C}$, is that

$$0 > \frac{dq}{d\psi} > -\nu_{\min}, \tag{4.4}$$

everywhere in $\mathbb{C}$, where $\nu_{\min} > 0$ is the minimum eigenvalue of the problem

$$\nabla^2\tilde{\varphi} + \nu\tilde{\varphi} = 0, \quad \text{in} \quad \mathbb{C}, \tag{4.5}$$

where $\tilde{\varphi}$ satisfies appropriate homogeneous or periodic boundary conditions. For an infinite zonal channel of width $M$, the eigenfunctions are given by

$$\tilde{\varphi} = e^{\pm i\alpha x} \sin\left(\frac{n\pi}{M} y\right),$$

for $n = 1, 2, 3, \cdots$, where $\alpha$ is a zonal wavenumber. The smallest $\nu_{\min}$ is given by $\alpha = 0$ and $n = 1$; that is,

$$\nu_{\min} = \left(\frac{\pi}{M}\right)^2.$$

If we set $M = 2667$ km (the north–south dimension of our subjectively chosen box-shaped block region), we obtain the value

$$\nu_{\min} = 1.4 \times 10^{-12}\ \text{m}^{-2}.$$

This value of $\nu_{\min}$ is shown on Fig. 10, together with the interior and exterior slopes of the least-squares $q(\psi)$ lines for each day.

It is evident that the condition (4.4), using our estimated $\nu_{\min}$, is never satisfied (see Fig. 10). Indeed, it is farthest from being met during the time when the block is strengthening and when it most resembles a dipole. The condition is closest to being satisfied from 8 to 11 February, which is the time in which the Omega block shows few closed contours, and the interior scatterplots (not shown) have a highly correlated $q(\psi)$ relation. Between 12 and 23 February, including the dipole stage, our results indicate that the condition (4.4) is even farther from being satisfied. It is tempting to make inferences about the stability of the two blocking configurations based on the times series presented in Fig. 10. This calculation would seem to suggest that the dipole configuration is farther from satisfying the stability condition in comparison to the Omega configuration (although neither satisfies it). If this is a correct interpretation of Fig. 10, then this may help to explain why dipole blocking configurations are often not observed over the northeast Pacific; and when they do occur they seem to have a relatively short lifetime. There are several shortcomings associated with making these inferences, and they should be pointed out here. Assuming, for the moment, that a constraint similar to (4.4) is applicable and that our calculation is qualitatively reasonable, the fact remains that *neither* configuration satisfies the constraint. It is likely not very meaningful to speak of their relative stability when both flow configurations are apparently unstable. Another obvious remark to make is that the stability condition (4.4) demands that the flow is *steady*. While we have argued here that the data suggest that the blocking episode is, comparatively speaking, a free mode, the fact of the matter is that there is undoubtedly an inherent time dependence. Another issue is, of course, just how much of what is observed corresponds to quasigeostrophic dynamics, which questions the applicability of (4.4) to the observed situation. Our intention here, in any event, is simply to suggest that it is likely that the relatively brief duration of the dipole configuration in comparison with the Omega configuration is related to their respective stability characteristics.

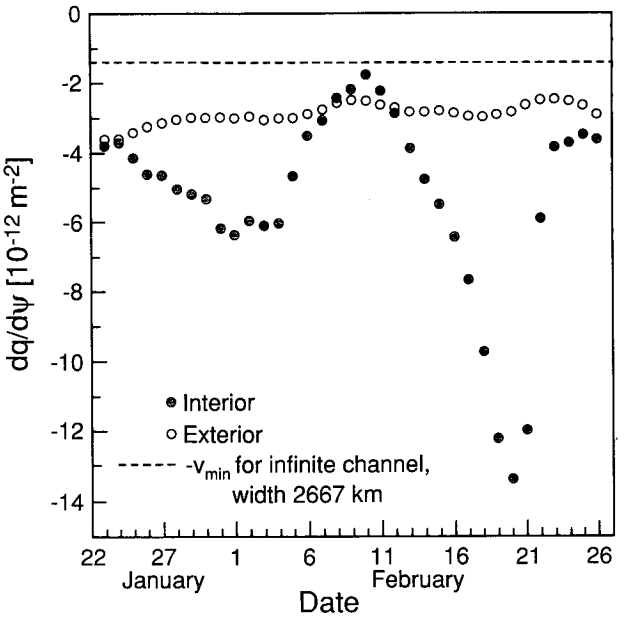


FIG. 10. The slopes of the least-squares 500-mb $q(\psi)$ lines. The estimated minimum slope for stability, $\nu_{\min}$, is given as a horizontal dashed line.

## 5. Conclusions

We have discussed a northeast Pacific blocking episode, using 5-day-mean 500-mb streamline charts as well as a series of scatter diagrams of geostrophic streamfunction versus vorticity. The block can be naturally divided into two stages, an Omega block stage (1–14 February) and a dipole stage (18–21 Febru-

ary). During both periods the scatter diagrams display an approximately linear relation between potential vorticity, $q$, and streamfunction, $\psi$. Scatter diagrams using *absolute* vorticity yield a similar conclusion.

The calculated net vorticity flux is relatively small during the time that the block is fully formed. From this, we conclude that this block may correspond to a free-mode solution of the governing (quasigeostrophic) equations, such solutions being characterized by a functional relation of the form $q = q(\psi)$. A time series of least-square estimated scatter diagram slopes $dq/d\psi$, when examined in the context of Arnol'd's second stability theorem, seems to suggest that the dipole configuration has less of a chance of being stable compared to the Omega configuration, particularly from 8 to 11 February. The suggested relative instability of the dipole form of the block is consistent with its relatively brief duration.

The scatterplots of 500-mb geostrophic streamfunction versus absoute vorticity are qualitatively quite similar to those with the potential vorticity. The similarity is slightly greater during the dipole stage than during the Omega block stage. We computed the root-mean-square contribution by the four lowest vertical normal modes to the eddy streamfunction within the blocking region.

The gravest vertical mode makes the greatest rms contribution. This is consistent with our observation that the scatterplots of absolute and potential vorticity are similar. The contribution of the gravest mode to the vertical structure increases as the Omega block develops, and remains at an elevated level for its duration. The three higher modes all show a tendency opposite to that of the gravest mode.

The decrease in the net vorticity flux (across the block region) preceding the formation of the Omega block can be physically identified with an intense synoptic-scale cyclonic system emerging out of the Arctic Ocean and tracking southeastward across the North American continent. This vortex is clearly distinguished on the scatter diagrams as a steepening of the plot between 27 January and 4 February. The same steepening effect during initial blocking development was observed by Malanotte-Rizzoli and Hancock (1987) in their composite of 12 North Atlantic blocking episodes.

We see some similarity between this intense vortex and the barotropic jet used by Flierl et al. (1983) to generate modons in the laboratory. We are led to speculate whether the strong anticyclonic shear on the southwestern flank of the vortex is analogous to the shear on the edge of the barotropic jet that creates the anticyclonic component of the laboratory modon. We consider it possible that this disturbance played the role of a nonlinear upscale forcing mechanism, described by Hansen and Chen (1982) as being crucial in the initial formation of some blocks. The scatter diagrams cannot show the details of the energy transfer that would verify this hypothesis. However, it appears that the net vorticity flux across the blocking region must decrease in time if the atmosphere is approaching a free mode. We speculate that blocks might be successfully forecast to form when significant decreases in net geostrophic vorticity flux across the preferred blocking region are caused by synoptic-scale systems that are associated with steepening of the $q(\psi)$ scatterplots.

The transition from the Omega to the dipole block is marked by a small increase in the baroclinicity, which we associated with the intense cyclonic vortices that are entrained into the block, forming the cyclonic component of the dipole. We conclude that the dipole block itself is just as barotropic as the Omega block but that both stages of the block appear to be initiated during brief periods of increased baroclinic activity.

Prior to the breakdown of the block, we again observe a steepening of the scatterplots, also associated with an intense cyclonic disturbance. However, this is not distinguished by any significant change in the net vorticity flux across the block, although the rms vertical mode time series shows a slight increase in baroclinic activity. Hence, our speculated forecast technique may not be applicable to the breakdown of blocks, but clearly it is risky to conclude too much from a single case study. A study of other blocking events using the same approach described in this paper would probably reduce some of the uncertainty in our conclusions.

*Acknowledgments.* This work was completed while NRE was on educational leave granted by the Atmospheric Environment Service of Canada. Preparation of this manuscript was supported in part by an Operating Research Grant awarded by the Natural Sciences and Engineering Research Council of Canada, and a Science Subvention awarded by the Atmospheric Environmental Service of Canada to GES.

## REFERENCES

Arfken, G., 1985: *Mathematical Methods for Physicists, 2nd edition.* Academic Press, 985 pp.

Arnol'd, V. I., 1966: On an a priori estimate in the theory of hydrodynamical stability. *Izvestiia Vysshikh Uchebnykh Zavednii Matematika,* **54,** 3–5 (in Russian). English translation, 1969: *AMS Trans. 2,* **79,** 267–269.

Baines, P. G., 1983: A survey of blocking mechanisms, with application to the Australian region. *Aust. Meteor. Mag.,* **31,** 27–36.

Butchart, N., K. Haines, and J. C. Marshall, 1989: A theoretical and diagnostic study of solitary waves and atmospheric blocking. *J. Atmos. Sci.,* **46,** 2063–2078.

Canadian Climate Centre, 1989: *Clim. Pers.,* **11,** nos. 1–9.

Canadian Meteorological Centre, 1989: *Monthly Review,* **5, May 1989.**

Derome, J., 1984: On quasi-geostrophic, finite-amplitude disturbances forced by topography and diabatic heating. *Tellus,* **36A,** 313–319.

Ek, N. R., 1992: Geostrophic scatter diagrams and the applicability of free mode theory to a Northeast Pacific Blocking Episode. M.Sc. thesis, Department of Geography, University of Alberta, Edmonton, Alberta, Canada, T6G 2G1, 123 pp.

Flierl, G. R., 1987: Isolated eddy models in geophysics. *Ann. Rev. Fluid Mech.,* **19,** 493–530.

——, V. D. Larichev, J. C. McWilliams, and G. M. Reznik, 1980: The dynamics of baroclinic and barotropic solitary eddies. *Dyn. Atmos. Oceans,* **5,** 1–41.

——, M. E. Stern, and J. A. Whitehead, 1983: The physical significance of modons: Laboratory experiments and general integral constraints. *Dyn. Atmos. Oceans,* **7,** 233–263.

Haines, K., 1989: Baroclinic modons as prototypes for atmospheric blocking. *J. Atmos. Sci.,* **46,** 3202–3218.

——, and J. C. Marshall, 1987: Eddy-forced coherent structures as a prototype of atmospheric blocking. *Quart. J. Roy. Meteor. Soc.,* **113,** 681–704.

Hansen, A. R., and T.-C. Chen, 1982: Spectral energetics analysis of atmospheric blocking. *Mon. Wea. Rev.,* **110,** 1146–1165.

Hildebrand, F. B., 1976: *Advanced Calculus for Applications,* 2d ed. Prentice-Hall, 733 pp.

Hogg, N. G., 1980: Effects of bottom topography on ocean currents. *Orographic Effects in Planetary Flows.* GARP Publ. Ser. No. 23, 167–265.

Holton, J. R., 1979: *An Introduction to Dynamic Meteorology,* 2d ed. Academic Press, 391 pp.

Hoskins, B. J., M. E. McIntyre, and A. W. Robertson, 1985: On the use and significance of isentropic potential vorticity maps. *Quart. J. Roy. Meteor. Soc.,* **111,** 877–946.

Larichev, V., and G. M. Reznik, 1976: Two-dimensional Rossby soliton: an exact solution. *Rep. U.S.S.R. Acad. Sci.,* **231**(5), 1077–1079.

McIntyre, M. E., and T. G. Shepherd, 1987: An exact local conservation theorem for finite-amplitude disturbances to non-parallel shear flows, with remarks on Hamiltonian structure and on Arnol'd's stability theorems. *J. Fluid Mech.,* **181,** 527–565.

McWilliams, J. C., 1980: An application of equivalent modons to atmospheric blocking. *Dyn. Atmos. Oceans,* **5,** 43–66.

Malanotte-Rizzoli, P., and P. J. Hancock, 1987: Coherent structures in a baroclinic atmosphere. Part IV: A comparison between theory and data. *J. Atmos. Sci.,* **44,** 2506–2529.

Malguzzi, P., and P. Malanotte-Rizzoli, 1984: Nonlinear stationary Rossby waves on nonuniform zonal winds and atmospheric blocking. Part I: The analytical theory. *J. Atmos. Sci.,* **41,** 2620–2628.

Mullen, S. L., 1986: The local balances of vorticity and heat for blocking anticyclones in a spectral general circulation model. *J. Atmos. Sci.,* **43,** 1406–1441.

——, 1987: Transient eddy forcing of blocking flows. *J. Atmos. Sci.,* **44,** 3–22.

Pedlosky, J., 1987: *Geophysical Fluid Dynamics,* 2d ed., Springer-Verlag, 710 pp.

Read, P. L., P. B. Rhines, and A. A. White, 1986: Geostrophic scatter diagrams and potential vorticity dynamics. *J. Atmos. Sci.,* **43,** 3226–3240.

Rex, D. F., 1950: Blocking action in the middle troposphere and its effect upon regional climate. I. An aerological study of blocking action. *Tellus,* **2,** 196–211.

Shutts, G. J., 1983: The propagation of eddies in diffluent jetstreams: eddy vorticity forcing of 'blocking' flow fields. *Quart. J. Roy. Meteor. Soc.,* **109,** 737–761.

——, 1986: A case study of eddy forcing during an Atlantic blocking episode. *Advances in Geophysics,* Vol. 29, Academic Press, 135–161.

Stern, M. E., 1975: Minimal properties of planetary eddies. *J. Mar. Res.,* **33,** 1–13.

Swaters, G. E., and L. A. Mysak, 1985: Topographically-induced baroclinic eddies near a coastline, with application to the Northeast Pacific. *J. Phys. Oceanogr.,* **15,** 1470–1485.

Warn, T., and B. Brasnett, 1983: The amplification and capture of atmospheric solitons by topography: A theory of the onset of regional blocking. *J. Atmos. Sci.,* **40,** 28–38.

Zauderer, E., 1989: *Partial Differential Equations of Applied Mathematics,* 2d ed. John Wiley & Sons, 891 pp.